DOI: 10.1002/ejic.200600337

A Cationic Order-Disorder Phase Transition in KPb_2Cl_5

Matias Velázquez,*[a] Alban Ferrier,[a] Olivier Pérez,[b] Stanislas Péchev,[c] Pierre Gravereau,[c] Jean-Pierre Chaminade,[c] and Richard Moncorgé[a]

Keywords: Halides / Solid-state structures / Structure elucidation / Phase transitions / Thermodynamics

The phase transition occurring at T_t = 528 K in the natural mineral and synthetic laser host compound KPb_2Cl_5 has been characterized by means of both single-crystal X-ray diffraction (XRD) as a function of temperature and differential scanning calorimetry (DSC). The K^+ and Pb^{2+}(2) cations order on passing from the high-temperature orthorhombic phase (space group *Pmcn*; a = 8.951, b = 8.015, c = 12.683 Å, Z = 4 at 623 K) to the low-temperature monoclinic one (space group $P2_1/c$; a = 8.849, b = 7.918, c = 12.472 Å, β = 90.11°, Z = 4, at room temperature), leading to a group-subgroup first-order phase transition displaying moderately fast kinetics and low entropy production upon thermal cycling around T_t. The positional entropy calculated from our crystal structure models corresponds to the transition entropy measured by DSC within the experimental error, and amounts to about 0.34 R. The driving force for the phase transition, $A \leq 22\ J\,mol^{-1}$, remains negligible with respect to both the thermal energy at T_t ($RT_t \approx 4.4\ kJ\,mol^{-1}$) and the transition latent heat ($\Delta H \approx 790\ J\,mol^{-1}$), thereby suggesting that this phase transition is a close-to-equilibrium process.

Introduction

KPb_2Cl_5 is a chloride[1] that has been known for a long time but has recently triggered a substantial body of literature because of its use as a host crystal for optical amplifiers in near- and middle-infrared solid-state lasers.[2] In this realm of applications, the growth of centimeter-sized high-quality single crystals is of paramount importance for several reasons. Firstly, it allows for the investigations of the intrinsic optical performances (grain boundaries and other microstructural defects can introduce passive losses within the laser cavity). Secondly, it permits the characterization of the anisotropy of these optical properties (absorption and emission cross-sections, for instance, can depend on the relative orientation of the electric field with respect to the optical axis of the crystal). Thirdly, it provides a means of concentrating a sufficiently large number of optically active ions with virtually no diffusion mobility within a cubic-centimeter-sized volume (with respect to gas lasers) to ensure optical amplification. In other respects, KPb_2Cl_5 occurs as a natural mineral named "challacolloite"[3] that readily forms in the flue dusts of steelmaking plants[4] and in the high-temperature fumarole gases of the Kudryavyi (Iturup Island, Kuril Islands), Vesuvius (Italy), and Satsuma–Iwojima (Japan) volcanoes.[3,5] Until now, the main crystal-growth method for elaborating pure and rare-earth-doped KPb_2Cl_5 single crystals has been the Bridgman–Stockbarger one: at least 20 different single crystals have been successfully elaborated by this method.[6–10] Powder X-ray diffraction (XRD) carried out at room temperature has established that KPb_2Cl_5 adopts the $NH_4Pb_2Cl_5$ structural type,[11] and a recent accurate refinement of single-crystal XRD data firmly confirmed this crystal structure.[12] Although several researchers have evoked the likelihood of a phase transition undergone by the crystals between the melting point and room temperature,[7,13] it is only recently that it was characterized by differential scanning calorimetry (DSC) and found to display a low entropy production per thermal cycle around T_t = 528.15 K.[10] In this paper we present a combined crystallographic and thermodynamic analysis of the phase transition in KPb_2Cl_5 by means of single-crystal XRD as a function of temperature and DSC experiments which supplement the ones previously undertaken. We demonstrate that it corresponds to a close-to-equilibrium cationic order-disorder group-subgroup first-order transition that displays moderately fast kinetics.

[a] Centre Interdisciplinaire de Recherche Ions Lasers, UMR 6637 CNRS/CEA/ENSICaen/Université de Caen,
6 Boulevard du Maréchal Juin, 14050 Caen cedex 04, France
Fax: +33-2-31452557
E-mail: matias.velazquez@ensicaen.fr
[b] Laboratoire de Cristallographie et Sciences des Matériaux, UMR 6508 CNRS/Université de Caen,
6 Boulevard du Maréchal Juin, 14050 Caen cedex 04, France
[c] Institut de Chimie de la Matière Condensée de Bordeaux, UPR 9048 CNRS,
87 Avenue du Docteur Albert Schweitzer, 33608 Pessac, France

Results and Discussion

Crystallographic Aspects

Both the room- and high-temperature structures consist of edge-sharing Pb^{2+}(1) monocapped octahedra that form

infinite chains along [100] (Figures 1 and 2). These are isolated from each other but surrounded by, and joined to, six $K^+/Pb^{2+}(2)$ face-sharing bicapped trigonal prism-based chains that also extend along the [100] direction (Figures 1 and 3). The K^+ and $Pb^{2+}(2)$ cations alternate in the room-temperature phase but are disordered in the high-temperature phase. The $K^+/Pb^{2+}(2)$ chains arrange in a pseudo-hexagonal network in the $(\bar{b}\bar{c})$ planes that contain the $Pb^{2+}(1)$ chains (Figure 4). Along [010], the $K^+/Pb^{2+}(2)$ polyhedra share one of their triangular faces, which gives rise to corrugated chains [with a 128.8° angle between three successive K^+ or $Pb^{2+}(2)$ cations] that are linked to each other by a Cl(5)–Cl(5) edge every three polyhedra (Figures 4 and 5). The $Pb^{2+}(1)$ monocapped octahedra share all their vertices but not more than one edge simultaneously with a neighboring K^+ and/or $Pb^{2+}(2)$ polyhedra. The two equatorial edges that are not linked to the $Pb^{2+}(1)$ polyhedra, along the [100] direction, are unshared. The three edges defining the triangular face at the opposite side from the capped face, as well as all the faces of the $Pb^{2+}(1)$ polyhedra, also remain unshared. In Figure 6 (a), the pseudo-quadrilateral face on the capped side has in common its four edges with the neighboring two K^+ and two $Pb^{2+}(2)$ polyhedra, which block the view of it. The rise in symmetry in the high-temperature phase stems from the fact that the K^+ and $Pb^{2+}(2)$ cations become equivalent, much like the (8d) K^+ cations do in K_2PrCl_5, which adopts the *Pnma* space group.[14] Hence, a mirror plane appears at 1/4,*y*,*z*, on which the $Pb^{2+}(1)$ cations are located (Figure 6). The 153.75° angle between the successive $Pb^{2+}(1)$ cations is virtually unaffected (155.6° at 623 K) by cationic ordering in the neighboring $K^+/Pb^{2+}(2)$ chains, whereas in the latter chains the angle between two consecutive K^+ and $Pb^{2+}(2)$ cations passes from 170.9° at room temperature to 180° at 623 K. Some of the structural parameters are quite sensitive to the phase transition. The analysis of the behavior of the unit-cell parameters (Figure 7) and of the diagonal coefficients of the anisotropic atomic displacement parameters (ADPs, presented in Figure 8) as a function of temperature is not devoid of interest for understanding the phase-transition mechanism. While the *a* and *b* parameters show a linear dependency on temperature from 293 to 573 K, the *c* parameter shows two breaks of slope at about 473 and 573 K, which provide clear evidence for the phase transition since they correspond to the initial and final peak temperatures in the C_p vs. T[10] and J_q vs. T curves (Figure 9). The

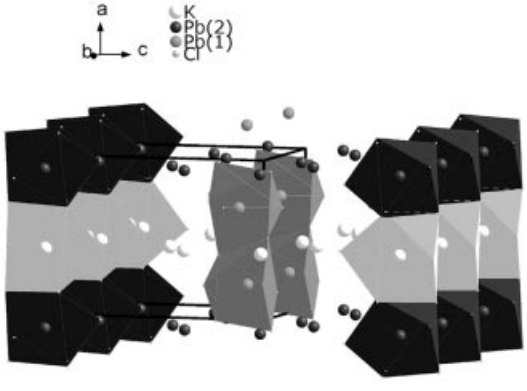

Figure 1. Simplified view of the KPb_2Cl_5 crystal structure at room temperature ($P2_1/c$) showing the two kinds of chains running along [100]: the ordered $K^+/Pb^{2+}(2)$ one and the $Pb^{2+}(1)$ one. In the high-temperature phase, the K^+ and $Pb^{2+}(2)$ cations become crystallographically equivalent and a cationic disorder appears in the $K^+/Pb^{2+}(2)$ chains over a length typically of 10–1000 Å (see text).

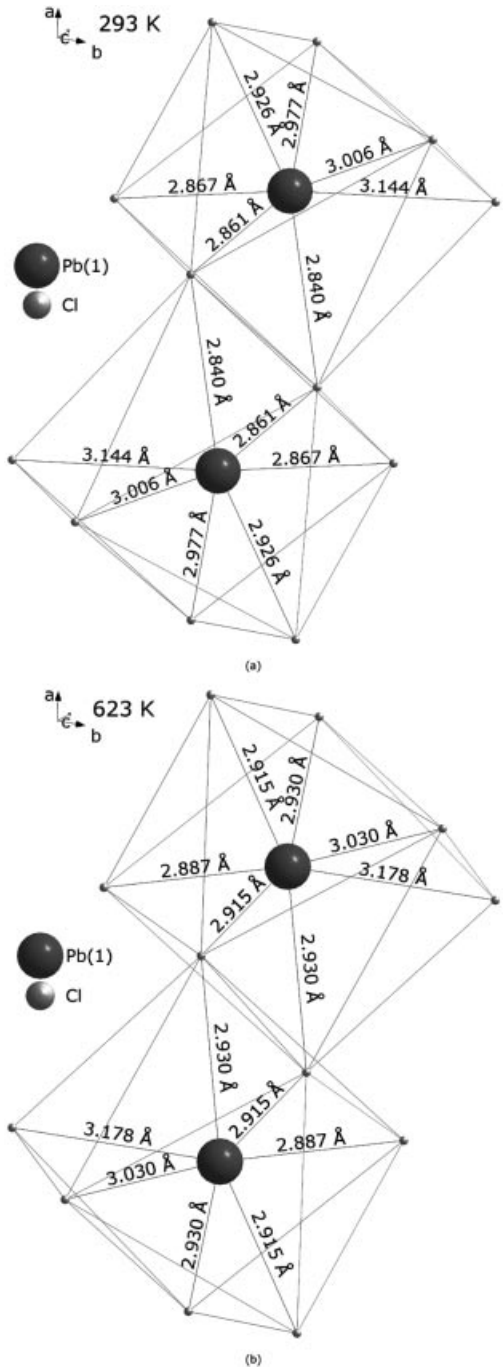

Figure 2. (a) Sketch of the $Pb^{2+}(1)$ chains in the room-temperature phase along [100]; (b) sketch of the $Pb^{2+}(1)$ chains at 623 K (*Pmcn* phase) along [100]. Both views show the edge-sharing of the monocapped octahedra.

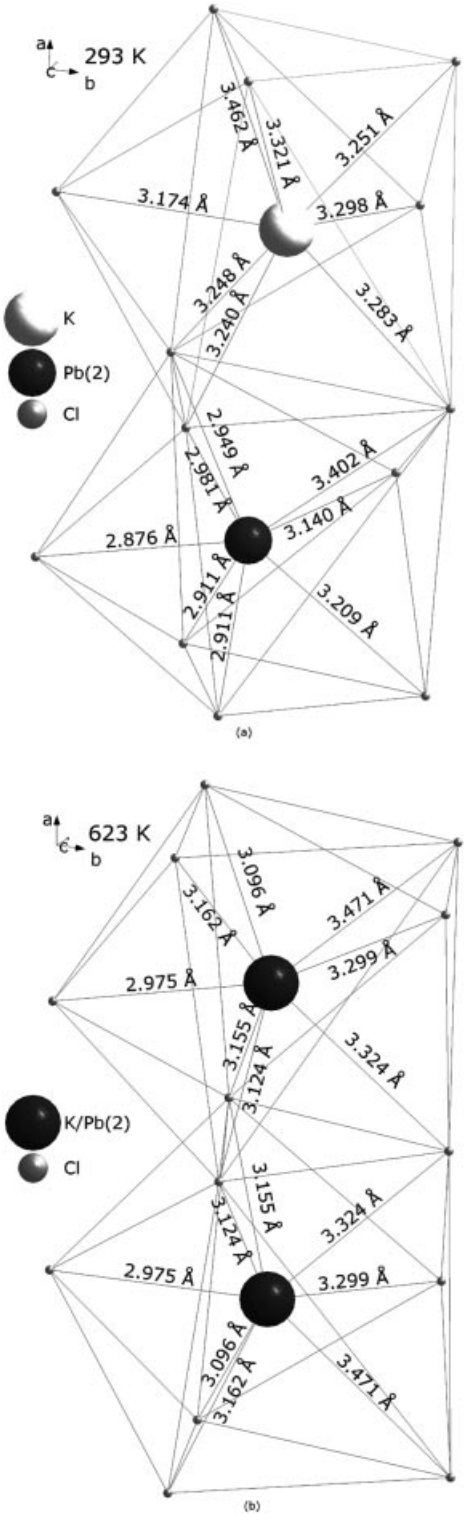

Figure 3. (a) Sketch of the ordered $K^+/Pb^{2+}(2)$ chains in the room-temperature phase along [100]; (b) sketch of the disordered $K^+/Pb^{2+}(2)$ chains at 623 K (*Pmcn* phase) along [100]. Both views show the triangular face-sharing of the bicapped trigonal prisms.

mean lattice-expansion coefficients are: $\frac{1}{a(293\text{ K})}\frac{da}{dT} \approx 38.6\times10^{-6}\text{ K}^{-1}$ (293–598 K), $\frac{1}{b(293\text{ K})}\frac{db}{dT} \approx 42.6\times10^{-6}\text{ K}^{-1}$ (293–598 K) and $\frac{1}{c(293\text{ K})}\frac{dc}{dT} \approx 39.3\times10^{-6}\text{ K}^{-1}$ (293–473 K). Although the lattice parameters' thermal expansion is not strictly equal to the thermal expansion tensor diagonal elements,[15] it provides a sufficiently accurate estimate of the latter quantities. Worthy of note is the patent decrease in the *c* parameter upon cooling, from 573 to 473 K $-\frac{1}{c(473\text{ K})}\frac{dc}{dT} \approx 97.9\times10^{-6}\text{ K}^{-1}$ − which suggests that in this temperature range the thermal stress may be substantial and also that a very slow cooling under an extremely flat temperature profile should be applied to the crystal to prevent the generation of dislocations in too large a concentration. The relative difference in unit cell volume between 293 K and the *Pmcn* phase at 623 K is about –3.9%. This anisotropic increase in lattice thermal expansion upon heating might be attributed to a larger density of weaker bonds along [001] than along the [100] and [010] directions. The K^+ and Pb^{2+} chloride polyhedral framework along [001] does not imply any single face-sharing, unlike along the [100] and [010] directions; however, the highest rises in U_{ii} values in the vicinity of the transition temperature occur along [100]. Analysis of the ADPs (Figure 8) supplies information about the possible diffusion paths for the K^+ and $Pb^{2+}(2)$ cations at high temperature. The doubling of the ADPs undergone by both K^+ and $Pb^{2+}(2)$ along the [100], [010] and [001] directions at the transition outlines the three-dimensional character of the diffusion of these two species. Moreover, the isotropy of the lattice thermal expansion up to 473 K, in conjunction with the interchain connections in the ($\vec{b}\vec{c}$) plane also indicate that the KPb_2Cl_5 structure possesses a good deal of three-dimensional character notwithstanding the existence of both ordered $K^+/Pb^{2+}(2)$ and $Pb^{2+}(1)$ chains in the room-temperature phase. The increase in the ADPs of the $Pb^{2+}(1)$ cations proves to be less marked than that of both K^+ and $Pb^{2+}(2)$. $Cl^-(1)$ shows a net rise in U_{33} between 473 and 548 K whereas in the other directions the thermal evolution of its ADPs seems regular. $Cl^-(2)$, but above all $Cl^-(5)$ and $Cl^-(3)$, displays a sharp increase in the displacement parameter along [100]. From the knowledge of the structure, three possible K/Pb(2) microscopic jumps can be conjectured: one along the [100] direction through the $Cl^-(3)$–$Cl^-(5)$–$Cl^-(2)$ triangular face, another one along [010] through the $Cl^-(1)$–$Cl^-(2)$–$Cl^-(3)$ triangular face (Figure 5) and the last one along [001] through the $Cl^-(5)$–$Cl^-(5)$ edge mentioned previously. The anisotropy of the ADPs' elongation [Figure 8 (b)] observed for $Cl^-(1)$ and $Cl^-(5)$ suggests a possible diffusion path along [001]. Indeed, this elongation occurs along [100] for $Cl^-(5)$, i.e. perpendicularly to the jump direction, and along [001] for $Cl^-(1)$, as sketched in Figure 5. Although these features are consistent with $K^+/Pb^{2+}(2)$ cation diffusion along the [001] direction, they are still speculative and call for a detailed energy-landscape calculation. Figure 10 illustrates how an XRD experiment can evidence the temperature spreading over about 100 K[10] of the phase transition: the *hk0* ($h + k = 2n + 1$) reflections observed at

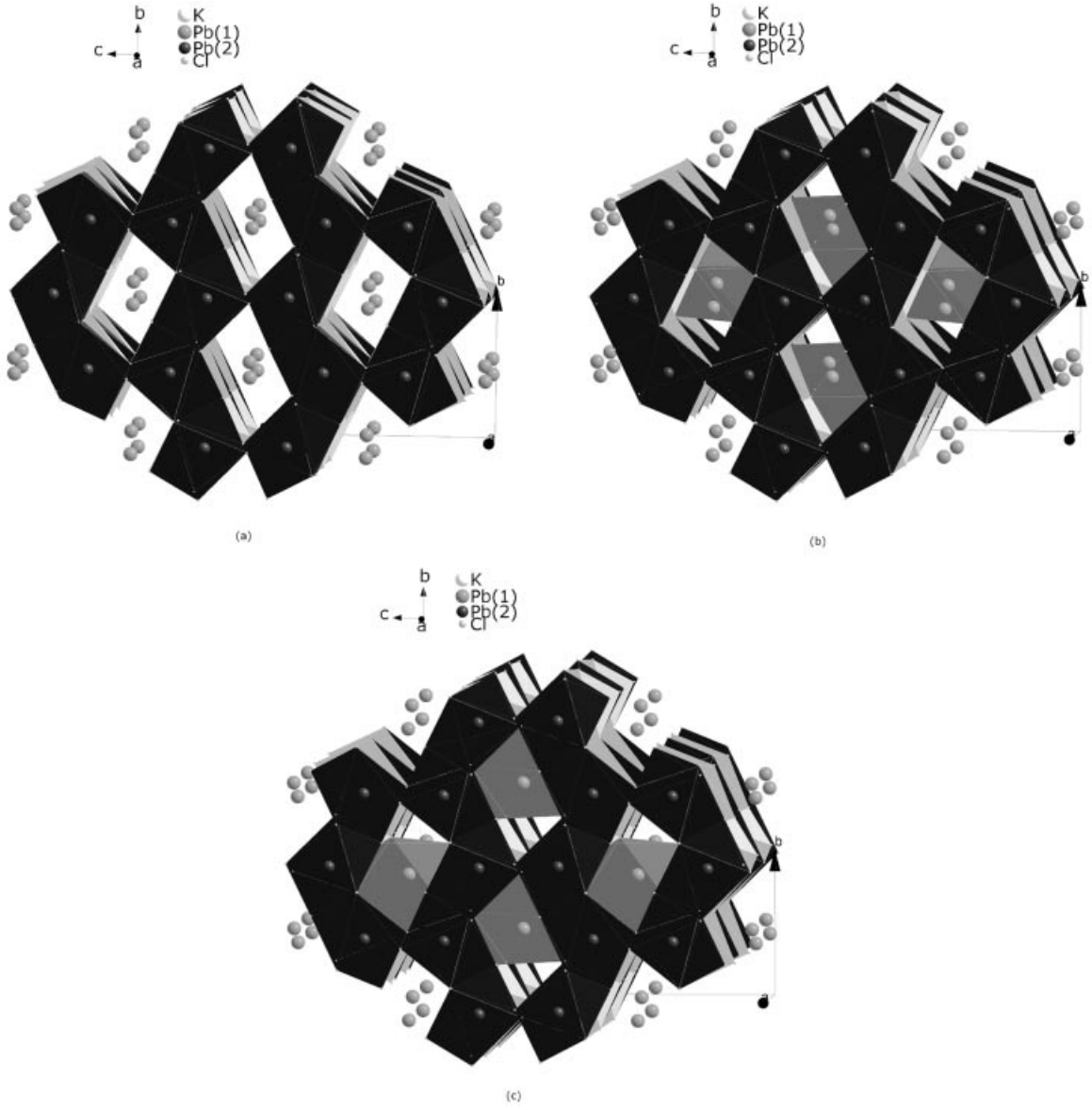

Figure 4. View of the KPb_2Cl_5 crystal structure at room temperature ($P2_1/c$) along [100] showing how the ordered $K^+/Pb^{2+}(2)$ chains share common edges in the ($\vec{b}\vec{c}$) planes to form a pseudo-hexagonal channel containing the $Pb^{2+}(1)$ chains: (a) without $Pb^{2+}(1)$ monocapped octahedra sketched; (b) with one $Pb^{2+}(1)$ monocapped octahedron drawn; (c) with the closest neighbor of the $Pb^{2+}(1)$ monocapped octahedron sketched in (b) drawn. These figures illustrate the zig-zag chains formed by the $Pb^{2+}(1)$ monocapped octahedra consistently with the 153.75° angle between three successive $Pb^{2+}(1)$ cations.

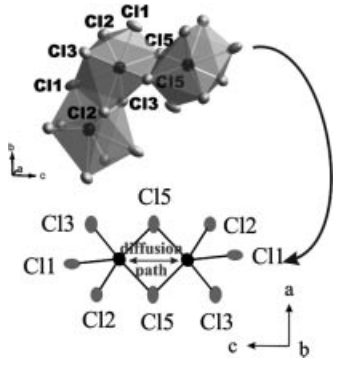

Figure 5. Speculative diffusion path for the K^+ and $Pb^{2+}(2)$ cations in KPb_2Cl_5 as deduced from the anisotropy of the Cl^- anions' thermal vibrations.

293 and 473 K transform, at first, at 548 K, into diffuse scattering and then vanish at 623 K. The occurrence of diffuse scattering is likely to be due to the $K^+/Pb^{2+}(2)$ cationic diffusion.

Structure of Rare-Earth Defects

Figures 6 (a) and (b) portray views of the $Pb^{2+}(1)$ polyhedron and chains that may prove useful when considering the local structure of the rare-earth defects that are liable to form when introduced within this compound to produce laser emission in the near- and middle-infrared wavelength range. In a recent work, we pointed out that the most expected rare-earth defects can be expressed in the Kröger–Vink notation as $RE^{\cdot}_{Pb} - V'_K$, $RE^{\cdot}_{Pb} - K'_{Pb}$, $RE^{\cdot\cdot}_K - V''_{Pb}$,

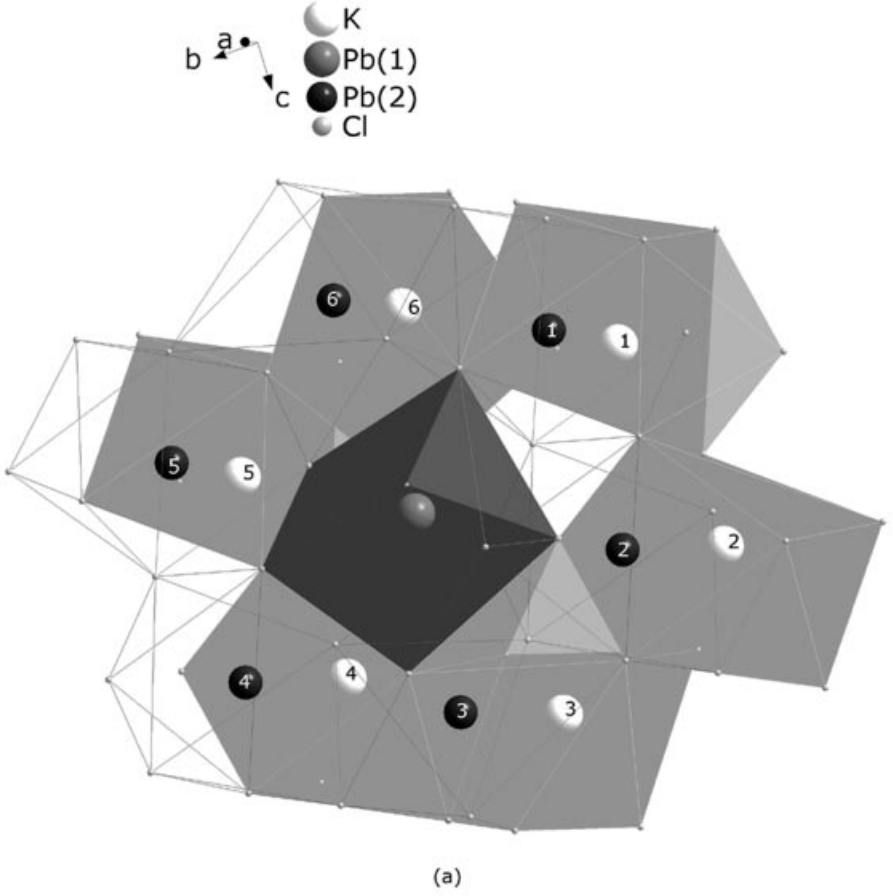

(a)

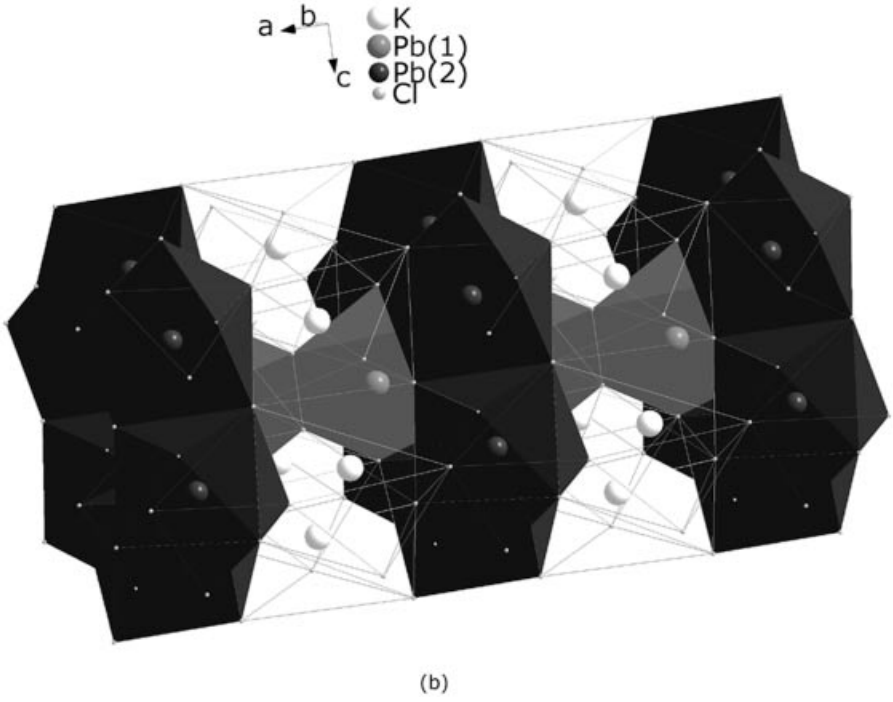

(b)

Figure 6. (a) Simplified view of the $Pb^{2+}(1)$ monocapped octahedron surrounded by six K^+ and $Pb^{2+}(2)$ polyhedra in the ($\bar{b}c$) planes; (b) simplified view of the isolated $Pb^{2+}(1)$ chains surrounded by six ordered $K^+/Pb^{2+}(2)$ chains in the room-temperature $P2_1/c$ phase. The labeling of the K^+ and $Pb^{2+}(2)$ sites indicates that they are symmetrically non-equivalent with respect to the $Pb^{2+}(1)$ sites.

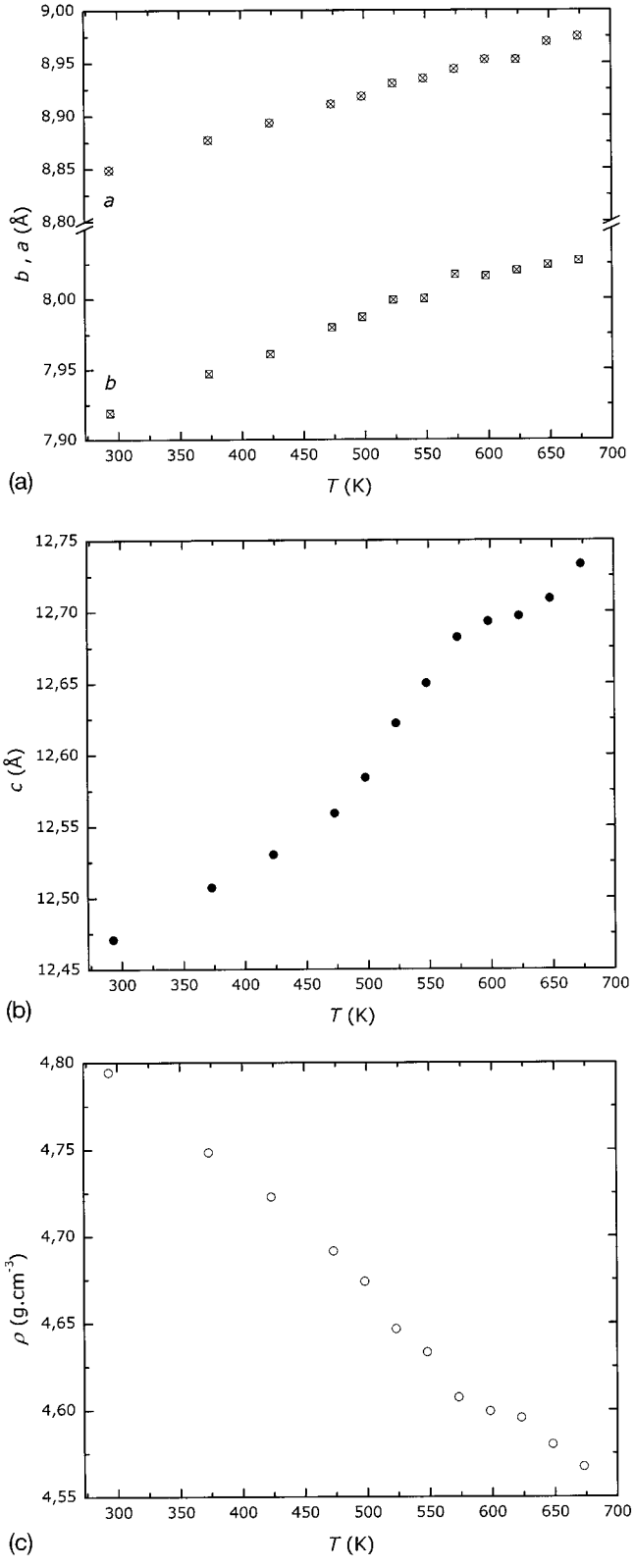

Figure 7. (a), (b) Thermal dependence of the KPb_2Cl_5 lattice parameters; (c) KPb_2Cl_5 "X-ray" volumic mass.

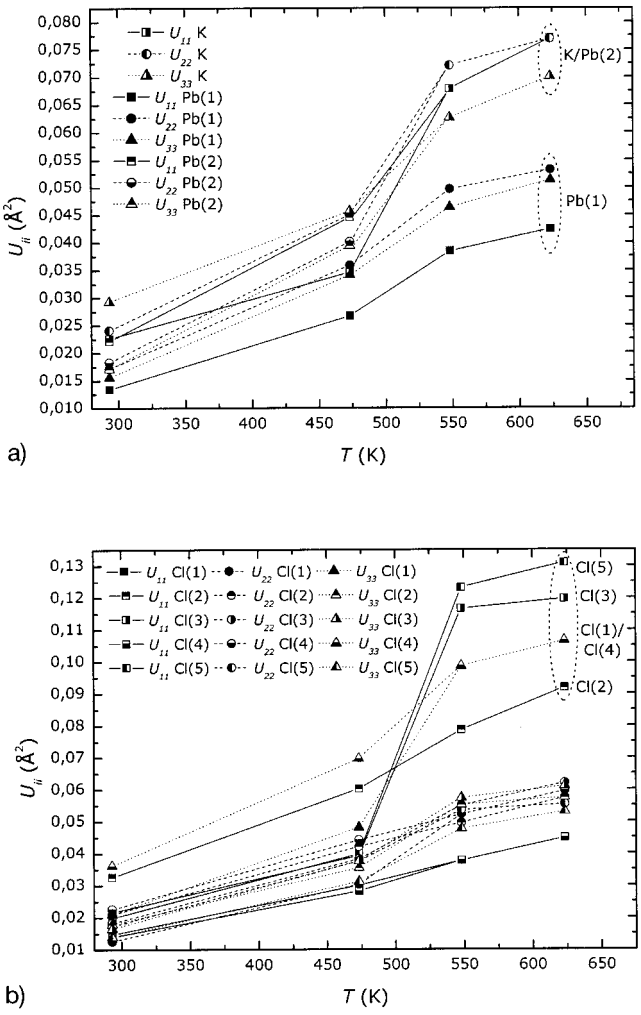

Figure 8. Refined diagonal elements of the anisotropic atomic displacement parameters for (a) the K^+ and Pb^{2+} cations and (b) the Cl^- anions in KPb_2Cl_5 at selected temperatures.

$RE^{\cdot}_{K} + 2V'_{K}$ and $2RE^{\cdot}_{Pb} + V''_{Pb}$. Let us now describe the situation more precisely by restricting our counting to nearest neighbors. There are six possible ways of forming each of the $RE^{\cdot}_{Pb(1)} - V'_{K}$, $RE^{\cdot}_{Pb(1)} - K'_{Pb(2)}$ and $RE^{\cdot}_{K} - V''_{Pb(1)}$ defects as the absence of symmetry elements makes all the nearest K^+ and $Pb^{2+}(2)$ neighbors symmetrically non-equivalent with respect to the $Pb^{2+}(1)$ sites. Along [100], there is only one possibility of finding the $RE^{\cdot}_{K} + V''_{Pb(2)}$ and $RE^{\cdot}_{Pb(2)} + V'_{K}$ defects. Owing to the inversion center located at 0,0,0 (right in the middle of the pseudo-hexagons drawn in Figure 4) three non-equivalent $RE^{\cdot}_{Pb(2)} + K'_{Pb(2)}$ defects can combine. The counting of three-center-type defects proves to be much more cumbersome, not only because of the lack of high-order symmetry elements [note, for example, thirty-six ways of forming $RE^{\cdot}_{Pb(2)} - V''_{Pb(2)} - RE^{\cdot}_{Pb(1)}$], but also because of the many possible combinations of $RE^{\cdot}_{Pb} - RE^{\cdot}_{Pb} - V''_{Pb}$. All in all, checking for the redundancies and with the proviso that the relaxation processes of atomic positions do not entail new symmetry element(s), this brings about more than 100 three-center defects in addition to the 23 two-center ones, all with a distinct formation free energy. Consequently, a distribution of

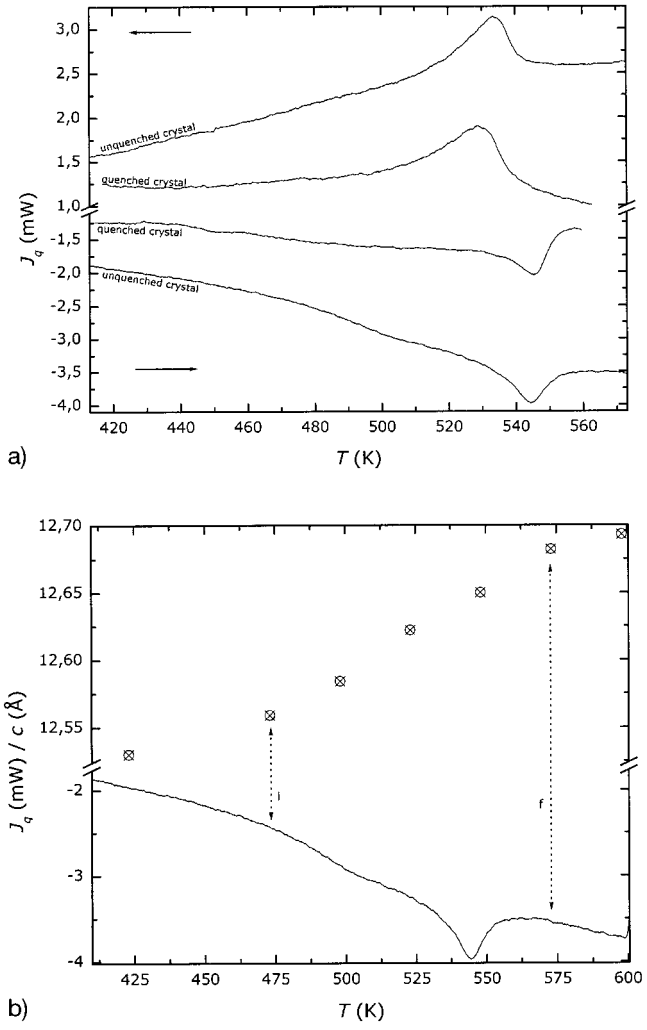

Figure 9. (a) Heat flux vs. temperature curves for raw KPb_2Cl_5 single crystals and KPb_2Cl_5 single crystals quenched from 633 K; (b) superposition of the unquenched KPb_2Cl_5 single crystal J_q vs. T and c vs. T curves. The double arrow labeled "i" indicates the initial peak temperature and that labeled "f" the final peak temperature.

them cannot be discarded a priori. It is even likely that the rare-earth defects' distribution depends on spatial coordinates because the formation free energy of a particular defect is affected by the concentration of its counterparts. These considerations put the recent attempts at characterizing the structure of rare-earth defects into perspective. A $Tb^{\cdot}_{Pb(1)} - V'_{K_4}$ defect, assumed to be the majority, has been supposed to account for the $^{159}Tb^{3+}$ high-frequency EPR spectra obtained in Tb^{3+}-doped KPb_2Cl_5 single crystals.[16] The labeling of the K^+ site is indicated in Figure 6 (a). By means of time-resolved fluorescence line-narrowing spectroscopy performed on Eu^{3+}-doped KPb_2Cl_5 single crystals, Cascales, Fernández and Balda concluded that three defects form, namely $Eu^{\cdot}_{Pb(2)} - V'_K$ (97%), $Eu^{\cdot}_{Pb(1)} - V'_{K_7}$ (1.9%) and $Eu^{\cdot\cdot}_K - V''_{Pb(?)}$ (1.1%), without unveiling which K^+ and Pb^{2+} sites are involved in the latter two defects.[17]

Thermodynamic and Kinetic Aspects

By making some assumptions, Defay and Prigogine established that the driving force of the transition should vary with time according to $A(t) = k\tau_r\cdot[1 - \exp(-t/\tau_r)]$.[18] Thus, during the phase transition, the value of the affinity A changes from 0 to approximately $k\tau_r$. We suggest to determine k according to $k \approx -\Delta H/\Delta t_t - \Delta V/V_m\cdot R\beta$, in which Δt_t, the time duration of the phase transition, can be obtained from the T vs. t DSC curve as the interval between the onset time of the baseline deviation and the time of the peak maximum; β, ΔV_m, and V_m stand for the temperature scanning rate, the molar volume contraction at fixed pressure and temperature, and some mean molar volume of the system in the vicinity of the transition, respectively. While the former is fixed by the experimenter, the latter can be estimated from the XRD data recorded around T_t. Our calorimetry and XRD data give $k \approx 11.6\,J\,mol^{-1}\,s^{-1}$. Furthermore, τ_r can be assigned an upper limit by a quenching experiment: this upper limit is τ_c, the intrinsic cooling time of a crystal and its container quenched from a temperature higher than T_t, provided that the quenched sample exhibits the phase transition exactly like the slowly cooled crystals (see Experimental Section). As $\tau_r \leq \tau_c \approx 1.9$ s, we deduce that $A \leq 22\,J\,mol^{-1}$. This value is of the same order of magnitude as the Gibbs free energy change we previously estimated with Smith's formula ($\Delta G \approx 35\,J\,mol^{-1}$).[10] The fact that the affinity remains smaller than both the latent heat ($\Delta H \approx 790\,J\,mol^{-1}$) and the thermal energy at T_t (ca. $4.4\,kJ\,mol^{-1}$), as well as the apparently fast energy relaxation kinetics and vanishingly small affinity threshold for the transition,[10] clearly indicate the close-to-equilibrium character of the transition, and are also consistent with its group-subgroup nature. The positional entropy can be approximated as $R\ln(x_{rt}/x_{ht})$, where x_{ht} and x_{rt} denote the number of atomic-position-independent parameters refined in the high-temperature phase (17) and in the room-temperature one (24), respectively. Hence, $\Delta S_{posn} = 0.345\,R \approx \Delta S_t$. In other words, this transition turns out to be an almost purely cationic order-disorder process, with virtually no phonon mode population redistribution or rotational disorder. Indeed, the extrapolation of the low-temperature part of the C_p vs. T curve falls into the high-temperature one.[10] This behavior of the specific heat baseline before and after the transition, and the fact that $\Delta S_t \approx \Delta S_{posn}$ lend support to the contention that $\Delta S_{vibr} \approx 0\,R$. Furthermore, as we were unable to detect any kind of collective tilt of the K^+ and Pb^{2+} polyhedra, we think that $\Delta S_{orient} = 0\,R$. Thus, the increase in U_{ii} values observed in Figure 8 certainly stems from the $K^+/Pb^{2+}(2)$ cations' positional disorder contribution to the Debye–Waller factor.[19] Assuming a K^+/Pb^{2+} lattice interdiffusion coefficient of the order of magnitude of 10^{-11}–$10^{-12}\,cm^2\,s^{-1}$ around T_t,[20] the fact that the same transition entropy is found in samples cooled from 633 K in about 1.9 s and in slowly cooled crystals leads us to presume that this cationic ordering takes place over a characteristic distance shorter than 1000 Å, that is, at the submesoscopic scale. On the other hand, owing to the ap-

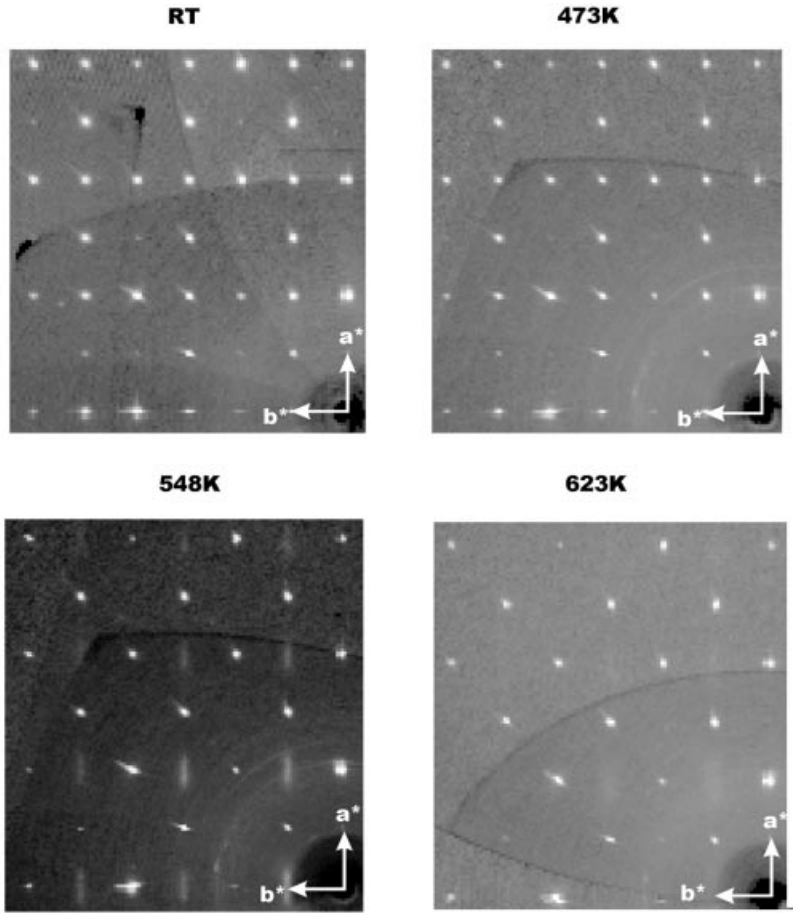

Figure 10. Plots of reciprocal lattice planes assembled from the series of experimental frames taken at various temperatures.

parently fast kinetics, low affinity, and group-subgroup nature of its phase transition, KPb_2Cl_5 is expected to belong to one of the two fully ferroelastic *mmmF*2/*m* species of Aizu's theory and display a 2×2 twinned domain microstructure.[21] The absence of splitting of the XRD spots (Figure 10) allows us to discard the possible coexistence of domains with different orientation states in the crystals of this study. This, in turn, suggests that the K^+/Pb^{2+} diffusion upon ordering happens over a length larger than the interatomic distance. Finally, we would like to mention that although the form of the KPb_2Cl_5 C_p vs. T curve around the transition and that of $NaClO_4$ in the vicinity of the orthorhombic *Cmcm* to cubic *Fm*3*m* transition temperature are as alike as two peas in a pod,[10,22] the latter situation proves to be fundamentally different because it involves rotational degrees of freedom of the perchlorate anions in the transition mechanism.

Conclusions

We have presented a consistent set of DSC and single-crystal XRD data that establishes the order-disorder group-subgroup phase transition occurring at 528 K in KPb_2Cl_5. This transition is of first order, displays moderately fast kinetics, and can be looked upon as a close-to-equilibrium process. In the high-temperature phase, a $K^+/Pb^{2+}(2)$ disorder takes place in the chains of bicapped trigonal prisms extending infinitely along the [100] direction. The lattice thermal expansion is almost isotropic from room temperature to about 473 K, but doubles its value along the [001] direction in the temperature range of the transition. We have also disentangled the connections between the $Pb^{2+}(1)$ chains embedded into the pseudo-hexagonal network of the $K^+/Pb^{2+}(2)$ chains.

Experimental Section

Synthesis and Crystal Growth: KCl powder (63.4 mmol, Chempur 99.99% used as received) was mixed with $PbCl_2$ powder (126.8 mmol, Chempur 99.999% used as received) in an agate mortar in a ca. 2% wet-nitrogen-filled glovebox, dried in vacuo, and heated in successive stages from 425 to 565 K under electronic-grade HCl gas in a silica tube (mounted to a 10^{-8} atm vacuum assembly), in order to promote the solid-state reaction taking place according to $KCl + 2\ PbCl_2 \xrightarrow[425–565\ K]{HCl} KPb_2Cl_5$. Details of the subse-

quent crystal growth by the Bridgman-Stockbarger method are given in ref.[10]

Quenching Procedure: Fresh KPb_2Cl_5 single crystals were taken from various locations of the bulk sample but neither from its beginning nor its end and sealed in a silica ampoule with a thickness of about 1 mm under 0.37 atm of HCl gas. The ampoule was placed in a vertical open furnace and heated at 633 K for 44 h. After this time, the ampoule was thrown into a mixture of ice and water. The intrinsic cooling time can be approximated to $\tau_{SiO_2} + \tau_{KPb_2Cl_5} \approx 1.9$ s, with $\tau_i = \frac{\rho_i C_p L_i^2}{M_i \kappa_i}$, $C_p(KPb_2Cl_5, 633\ K) \approx 40.3\,R$[10] and $\kappa(KPb_2Cl_5, 300\ K) \approx 4.62\ W\,m^{-1}\,K^{-1}$,[23] provided that the surface exchange contributions to heat dissipation can be neglected. The crystals did not seem to undergo mechanical breakdown upon quenching.

Differential Scanning Calorimetry: Calorimetric measurements were performed from room temperature to 600 K at a temperature variation rate of $\beta = \pm 10\ °C\,min^{-1} \approx \pm 167\ mK\,s^{-1}$, with a commercial continuous disk-type heat flux differential scanning calorimeter. A piece of fresh KPb_2Cl_5 crystal ($m = 34.3 \pm 0.2$ mg), and a quenched specimen ($m = 38.3 \pm 0.2$ mg) were placed without grinding into a stainless-steel crucible in a ca. 2% wet-nitrogen-filled glovebox. The crucibles were then sealed with a stainless-steel top and an Ni ring designed to resist pressures of around 100 atm at 873.15 K. The calorimetry cell was continuously purged with 4N5 N_2 gas. Temperature and caloric calibrations are explained in ref.[10] The results are shown in Figure 9 (a).

Crystal Structure: The XRD investigation was performed at different temperatures (293, 473, 548, and 623 K), with Mo-K_α radiation, with a Kappa CCD (Bruker Nonius) diffractometer equipped with a Cyberstar gas blower system. Large Ω- and Φ-scans were used to control both the crystalline quality of different samples and determine the unit-cell parameters. A single crystal of suitable size ($100 \times 150 \times 150$ μm) was then selected. The dependency of the cell parameters on the temperature was obtained from large Ω- and Φ-scans performed at different temperatures; the results are reported in Figures 7 (a–c). The evolution of the *c* parameter allowed us to probe the structural transition and fix the most adequate temperature for the data collection process. Suitable data-collection strategies were defined by considering the cell parameters, the spot size, and the obstruction of the diffractometer by the high-temperature conditioning apparatus. For the room-temperature measurement, a scanning angle of 0.8° and a *Dx* (detector–sample distance) of 55 mm were chosen; Φ- and Ω-scans were used. To collect a large number of weak reflections, but avoiding any detector saturation by reflections of strong intensity, two different exposure times (45 s/° and 5 s/°) were used to collect the data. The diffracted intensities were collected up to $\theta = 42°$. One independent monoclinic space was scanned. Plots of reciprocal lattice planes assembled from these series of experimental frames are sufficiently accurate to obtain an overall view of the reciprocal space. The diffraction pattern can be described within a monoclinic cell [cell parameters $a = 8.8492(3)$, $b = 7.9183(5)$, $c = 12.4716(7)$ Å, $\beta = 90.106(3)°$]. The observed conditions limiting the possible reflections, *h0l*: $l = 2n$ and *0k0*: $k = 2n$, are consistent with the $P2_1/c$ space group. The measurements at high temperatures are more tedious. The presence of both the conditioning apparatus and the high-temperature gas flow modifies the environment of the goniometer and generates new shadow zones. To decrease the obstruction near the sample and to avoid collisions or a direct contact of the gas flow with the detector, *Dx* was fixed at 60 mm and only Φ-scans were used. All data collections at high temperatures were undertaken according

Table 1. Details of XRD data and structure refinements for KPb_2Cl_5 at selected temperatures.

	293 K	473 K	548 K	623 K
Empirical formula	KPb_2Cl_5	KPb_2Cl_5	KPb_2Cl_5	KPb_2Cl_5
Crystal system	monoclinic	monoclinic	orthorhombic	orthorhombic
Space group	$P2_1/c$ (no. 14)	$P2_1/c$ (no. 14)	*Pmcn* (no. 62)	*Pmcn* (no. 62)
Z	4	4	4	4
Formula mass [g mol^{-1}]	630.743	630.743	630.743	630.743
F(000)	1072	1072	1072	1072
Radiation	Mo-K_α (λ = 0.71073 Å)	Mo-K_α (λ = 0.71073 Å)	Mo-K_α (λ = 0.71073 Å)	Mo-K_α (λ = 0.71073 Å)
Crystal size [mm]	0.10×0.15× 0.15	0.10×0.15× 0.15	0.10×0.15× 0.15	0.10×0.15× 0.15
Diffractometer: Enraf–Nonius	Kappa CCD	Kappa CCD	Kappa CCD	Kappa CCD
Monochromator	graphite	graphite	graphite	graphite
θ range [°]	2–42	2–35	2–35	2–35
Index ranges	$-16 \le h \le 16$	$-10 \le h \le 10$	$0 \le h \le 14$	$0 \le h \le 14$
	$0 \le k \le 14$	$0 \le k \le 12$	$0 \le k \le 12$	$0 \le k \le 12$
	$0 \le l \le 23$	$0 \le l \le 20$	$0 \le l \le 20$	$0 \le l \le 20$
Scan type	φ and ω	φ	φ	φ
Independent reflections	6083	2040	1383	1384
Reflections with $I > 3\sigma(I)$	4335	1575	807	819
R_{int} (%)	4.18	3.05	2.95	3.50
Refinement method	full-matrix least squares on F^2			
Parameters refined	75	75	45	45
Weighting scheme	$w = 1/[\sigma^2(F_o^2) + (\alpha P)^2 + \beta P]$, $P = (F_o^2 + 2F_c^2)/3$			
Absorption correction	SADABS	SADABS	SADABS	SADABS
Extinction coefficient	0.108(2)	–	0.052(5)	0.101(7)
Goodness-of-fit on F^2	1.38	1.77	4.7	3.5
Final *R* factor				
R_1 [$I > 3\sigma(I)$]	0.028	0.029	0.049	0.046
wR_2 [$I > 3\sigma(I)$]	0.023	0.026	0.041	0.039
Max. shift/esd	0.005	0.002	0.0001	0.0002
Largest diff. peaks and holes [e Å^{-3}]	+2 [0.50 Å near Pb(1)]	+1.4 (0.70 Å near K)	+3.25 [1 Å near Pb(1)]	+2.33 [0.30 Å near Pb(2)/K]
	–2 [0. 55 Å near Pb(2)]	–1.3 [0. 4 Å near Pb(1)]	–3.25 [0. 35 Å near Pb(2)/K]	–3.05 [0. 40 Å near Pb(2)/K]

to the procedure reported in Table 1. The conditions limiting the possible reflections at 473 K are the one observed at room temperature, but at 548 and 623 K new conditions consistent with the *Pmcn* space group appear (*h0l*: $l = 2n$ and *hk0*: $h + k = 2n$; see Figure 10). At 623 K, the cell parameters are $a = 8.851(12)$, $b = 8.015(17)$, $c = 12.683(15)$ Å. It should be noted that *Pmcn* is a supergroup of $P2_1/c$. The existence of diffuse scattering centered on the nodes *hk0*: $h + k = 2n + 1$ in Figure 10 at 548 K should be noted. The EvalCCD software[24] was used to extract reflections from the collected frames and reflections were merged and rescaled as a function of the exposure time. Data were corrected from absorption using the SADABS program[25] developed for scaling and correction of area-detector data. At room temperature a structural model considering the $P2_1/c$ space group was built up with SIR2002[26] using direct methods. Then, the cations and the chloride anions were located. This model was subsequently introduced in the refinement program Jana2000,[27] all the atomic positions were refined, and finally anisotropic atomic displacement parameters were considered for all the atoms. The refinement led to an agreement factor of 2.8%.

It should be noted that the room-temperature data collection and refinement were performed using two different single crystals of the same batch, which gave the same results and that, in particular, none of the crystals investigated were twinned. The structure at 473 K, which exhibits a monoclinic symmetry, was refined using the final result of the room-temperature structure. Except for the ADPs, no significant modifications in the structure were observed (Table 2). The refinements of the structure at higher temperatures were carried out using a model generated in the *Pmcn* space group from the atomic positions determined at room temperature. One should bear in mind that, in the *Pmcn* symmetry, the $Cl^-(1)$ and $Cl^-(4)$ anions as well as the K^+ and $Pb^{2+}(2)$ cations become equivalent (Table 2). The behavior of the ADPs as a function of T is displayed in Figure 8 (a) and (b). Further details of the crystal structure investigations may be obtained from the Fachinformationzentrum Karlsruhe, 76344 Eggenstein-Leopoldshafen, Germany [Fax: +49-7247-808-666; E-mail: crysdata@fiz-karlsruhe.de] on quoting the depository numbers CSD-416430 (293 K), -416431 (473 K), -416432 (548 K), and -416433 (623 K).

Table 2. Refined atomic coordinates for KPb_2Cl_5 at room temperature ($P2_1/c$ phase) and 623 K (*Pmcn* phase).

293 K Atom	Wyckoff position	x	y	z
K	4e	0.50993(10)	0.55118(12)	0.83129(7)
Pb(1)	4e	0.745007(14)	0.064158(17)	0.993373(10)
Pb(2)	4e	0.006756(16)	0.506409(19)	0.825856(11)
Cl(1)	4e	0.04196(9)	0.16588(11)	0.90205(7)
Cl(2)	4e	0.77048(12)	–0.15544(13)	0.81152(8)
Cl(3)	4e	0.76408(10)	0.31165(12)	0.72073(7)
Cl(4)	4e	0.54059(10)	–0.17941(13)	0.08070(9)
Cl(5)	4e	0.77812(10)	0.45939(12)	0.99858(7)
623 K Atom	**Wyckoff position**	x	y	z
Pb(1)	4c	0.25	0.05955(6)	–0.00625(3)
K/Pb(2)	8d	0.50103(7)	–0.48274(8)	–0.17144(6)
Cl(1)/Cl(4)	8d	0.4616(2)	–0.1721(3)	0.0892(2)
Cl(2)	4c	0.75	–0.1845(4)	–0.2192(3)
Cl(3)	4c	0.25	–0.1539(4)	–0.1896(3)
Cl(5)	4c	0.25	0.4560(4)	–0.0004(2)

Table 3. Selected bond lengths [Å] for KPb_2Cl_5 in the room-temperature ($P2_1/c$) and high-temperature (*Pmcn*) phases.

293 K[a]					
Pb(1)–Cl(1)^{i}	2.9770(8)	Pb(2)–Cl(1)	2.8756(9)	K–Cl(2)^{xi}	3.2826(14)
Pb(1)–Cl(1)^{ii}	2.9263(8)	Pb(2)–Cl(1)^{vi}	3.1393(9)	K–Cl(2)^{viii}	3.4625(13)
Pb(1)–Cl(2)	2.8671(10)	Pb(2)–Cl(2)^{vii}	3.4016(10)	K–Cl(3)	3.2509(13)
Pb(1)–Cl(3)^{iii}	3.0058(9)	Pb(2)–Cl(2)^{viii}	2.9114(10)	K–Cl(3)^{viii}	3.2477(13)
Pb(1)–Cl(4)^{iv}	2.8610(10)	Pb(2)–Cl(3)^{ix}	2.9492(9)	K–Cl(4)^{v}	3.1737(14)
Pb(1)–Cl(4)^{v}	2.8398(9)	Pb(2)–Cl(3)^{viii}	3.2087(9)	K–Cl(4)^{iii}	3.2978(14)
Pb(1)–Cl(5)	3.1438(9)	Pb(2)–Cl(5)^{ix}	2.9815(8)	K–Cl(5)	3.2396(12)
		Pb(2)–Cl(5)^{x}	2.9113(8)	K–Cl(5)^{x}	3.3207(12)
623 K[b]					
Pb(1)–Cl(5)	3.179(3)		K/Pb(2)–Cl(5)^{iv}	3.161(2)	
Pb(1)–Cl(1) (×2)	2.916(2)		K/Pb(2)–Cl(5)^{i}	3.1246(19)	
Pb(1)–Cl(1)^{i} (×2)	2.930(2)		K/Pb(2)–Cl(1)^{v}	2.976(2)	
Pb(1)–Cl(2)^{i}	3.030(3)		K/Pb(2)–Cl(1)^{vi}	3.298(3)	
Pb(1)–Cl(3)	2.887(3)		K/Pb(2)–Cl(2)	3.324(3)	
			K/Pb(2)–Cl(2)^{vii}	3.096(2)	
			K/Pb(2)–Cl(3)	3.471(2)	
			K/Pb(2)–Cl(3)^{vii}	3.155(2)	

[a] i: $1 - x, -y, -z$; ii: $1 - x, -y, 2 - z$; iii: $x, 1/2 - y, 1/2 + z$; iv: $-x, -y, 1 - z$; v: $1 - x, -y, 1 - z$; vi: $x, 1/2 - y, 3/2 + z$; vii: $-1 - x, 1 - y, -z$; viii: $1 + x, 1/2 - y, 3/2 + z$; ix: $-1 - x, -y, -z$; x: $1 - x, 1 - y, 2 - z$; xi: $-x,1 - y, -z$. [b] i: $1 - x, -y, -z$; ii: $-1/2 - x, y, z$; iii: $1/2 - x, y, z$; iv: $-x, -1 - y, -z$; v: $1 - x, -1 - y, -z$; vi: $-x, -1/2 + y, -1/2 - z$; vii: $1 - x, -1/2 + y, -1/2 - z$.

Acknowledgments

A. F. is the holder of a PhD thesis DGA fellowship from the French Ministry of Defense. This work was partly supported by the Centre National de la Recherche Scientifique (CNRS) and the Conseil Régional de Basse-Normandie. We would like to acknowledge Miss Hélène Rousselière for her technical help during the high-temperature XRD measurements.

[1] R. Lorenz, W. Ruckstuhl, *Z. Anorg. Chem.* **1907**, *51*, 71–89.
[2] L. I. Isaenko, A. P. Yelisseyev, A. M. Tkachuk, S. E. Ivanova, S. A. Payne, R. H. Page, M. C. Nostrand, *Proc. SPIE – Int. Soc. Opt. Eng.* **2002**, *4900*, 962–972.
[3] J. Schlüter, D. Pohl, S. Britvin, *Neues Jahrb. Mineral., Monatsh.* **2005**, *182*, 95–101.
[4] H. M. Artelt, E. Greinacher, G. Meyer, *J. Prakt. Chem.* **1993**, *335*, 255–261.
[5] S. I. Tkachenko, R. P. Porter, M. A. Korzhinskii, M. D. Van Bergen, K. I. Shmulovich, G. S. Shteinberg, *Geokhimiya* **1999**, *4*, 410–422.
[6] M. Voda, M. Al-Saleh, G. Lobera, R. Balda, J. Fernández, *Opt. Mater.* **2004**, *26*, 359–363.
[7] K. Nitsch, M. Dušek, M. Nikl, K. Polák, M. Rodová, *Prog. Cryst. Growth Charact.* **1995**, *30*, 1–22.
[8] U. N. Roy, Y. Cui, M. Guo, M. Groza, A. Burger, G. J. Wagner, T. J. Carrig, S. A. Payne, *J. Cryst. Growth* **2003**, *258*, 331–336.
[9] L. Isaenko, A. Yelisseyev, A. Tkachuk, S. Ivanova, S. Vatnik, A. Merkulov, S. Payne, R. Page, M. Nostrand, *Mater. Sci. Eng. B* **2001**, *81*, 188–190.
[10] M. Velázquez, A. Ferrier, J.-P. Chaminade, B. Menaert, R. Moncorgé, *J. Cryst. Growth* **2006**, *286*, 324–333.
[11] H. P. Beck, G. Clicqué, H. Nau, *Z. Anorg. Allg. Chem.* **1986**, *536*, 35–44.
[12] A. A. Merkulov, L. I. Isaenko, V. M. Pashkov, V. G. Mazur, A. V. Virovets, D. Ju. Naumov, *J. Struct. Chem.* **2005**, *46*, 103–108.
[13] K. Nitsch, A. Cihlář, Z. Malková, M. Rodová, M. Vaněček, *J. Cryst. Growth* **1993**, *131*, 612–615.
[14] G. Meyer, J. Soose, A. Moritz, V. Vitt, Th. Holljes, *Z. Anorg. Allg. Chem.* **1985**, *521*, 161–172.
[15] R. O. Simmons, R. W. Balluffi, *Phys. Rev.* **1960**, *119*, 600–605.
[16] G. S. Shakurov, B. Z. Malkin, A. R. Zakirov, A. G. Okhrimchuk, L. N. Butvina, N. V. Lichkova, V. N. Zavgorodnev, *Appl. Magn. Reson.* **2004**, *26*, 579–586.
[17] C. Cascales, J. Fernández, R. Balda, *Opt. Express* **2005**, *13*, 2141–2152.
[18] R. Defay, I. Prigogine, in *Thermodynamique Chimique*, 2nd ed., Éditions Desoer, Liège, Éditions Dunod, Paris, **1950**.
[19] W. F. Kuhs, in *International Tables for Crystallography*, vol. D ["Physical properties of crystals", chapter 1.9 ("Atomic displacement parameters")] (Ed.: A. Authier), Kluwer Academic Publishers, Dordrecht, Boston, London, **2003**, pp. 228–242.
[20] G.-M. Schwab, R. Deml, *Z. Phys. Chem. (Muenchen, Ger.)* **1964**, *42*, 280–292.
[21] K. Aizu, *Phys. Rev. B* **1970**, *2*, 754–772.
[22] K. O. Strømme, *Acta Chem. Scand. A* **1974**, *28*, 515–527.
[23] A. M. Tkachuk, S. E. Ivanova, L. I. Isaenko, A. P. Yelisseyev, M.-F. Joubert, Y. Guyot, S. Payne, *Opt. Spectr.* **2003**, *95*, 722–740.
[24] A. Duisenberg, L. Kroon-Batenburg, A. Shreurs, *J. Appl. Crystallogr.* **2003**, *36*, 220.
[25] G. M. Sheldrick, *SADABS, program for scaling and correction of area detector data*, Göttingen, Germany, **1997**.
[26] M. Burla, M. Camalli, B. Carrozzini, G. L. Cascarano, C. Giacovazzo, G. Polidori, R. Spagna, *SIR2002*, Institute of Crystallography, Bari, Italy, **2002**.
[27] V. Petricek, M. Dusek, *Jana 2000, The crystallographic computing system*, Institute of Physics, Praha, Czech Republic, **2000**.

Received: April 16, 2006
Published Online: August 9, 2006

